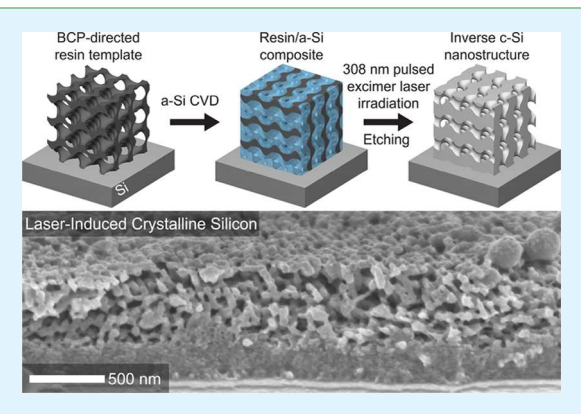


Synthesis and Formation Mechanism of All-Organic Block Copolymer-Directed Templating of Laser-Induced Crystalline Silicon Nanostructures

Kwan Wee Tan,^{†,‡} Jörg G. Werner,[†] Matthew D. Goodman,[§] Ha Seong Kim,[§] Byungki Jung,[†] Hiroaki Sai,[†] Paul V. Braun,[§] Michael O. Thompson,[†] and Ulrich Wiesner*,[†]

Supporting Information

ABSTRACT: This report describes the generation of three-dimensional (3D) crystalline silicon continuous network nanostructures by coupling all-organic block copolymer self-assembly-directed resin templates with low-temperature silicon chemical vapor deposition and pulsed excimer laser annealing. Organic 3D mesoporous continuous-network resin templates were synthesized from the all-organic self-assembly of an ABC triblock terpolymer and resorcinol-formaldehyde resols. Nanosecond pulsed excimer laser irradiation induced the transient melt transformation of amorphous silicon precursors backfilled in the organic template into complementary 3D mesoporous crystalline silicon nanostructures with high pattern fidelity. Mechanistic studies on laserinduced crystalline silicon nanostructure formation revealed that the resin template was carbonized during transient laser-induced heating on the milli- to nanosecond timescales, thereby imparting enhanced



thermal and structural stability to support the silicon melt-crystallization process at temperatures above 1250 °C. Photoablation of the resin material under pulsed excimer laser irradiation was mitigated by depositing an amorphous silicon overlayer on the resin template. This approach represents a potential pathway from organic block copolymer self-assembly to alternative functional hard materials with well-ordered 3D morphologies for potential hybrid photovoltaics, photonic, and energy storage applications.

KEYWORDS: self-assembly, laser heating, 3D silicon nanostructure, block copolymers, templating

INTRODUCTION

Casting is one of the most ubiquitous and oldest processes in the world to shape materials, appearing as early as the Bronze Age. For instance, the earliest work discovered is that of a copper frog casted around 3200 B.C. in the ancient Mesopotamia region. Today, casting processes continue to dominate manufacturing industries that fabricate complex shapes of metals, ceramics, and polymeric materials for various applications, ranging from automotive and plumbing to engine components. Typically, during casting, the casted material is melted and filled into arbitrarily shaped cavities in the mold, followed by solidification and removal of the mold. As a prerequisite, the mold material has to be physically and chemically stable under the processing conditions of the casted melt and therefore typically possesses a higher melting temperature and enhanced corrosion resistance.

Today, even at the smallest length scales, casting provides viable pathways to fabricate periodically ordered three-

dimensional (3D) nano- to mesostructured materials, such as photonic crystals or metamaterials,²⁻⁷ for use in current and emerging applications, 1,8-10 including catalysis 11,12 and energy conversion and storage. 13-17 In particular, block copolymer (BCP) self-assembly-directed templating enables formation of well-defined complex morphologies, such as the periodically ordered 3D continuous gyroidal mesostructures. 9,10 In the "soft" templating approach, structure-directing BCPs can be combined with organic/inorganic additives or nanoparticles to form periodically ordered porous structures with mesoscopic (2-50 nm) and larger length scale features. 16-25 The porous organic/inorganic BCP structure can be further utilized as a "hard" template for backfilling with an alternative material, followed by etching, to yield functional structures with the

Received: July 26, 2018 Accepted: November 16, 2018 Published: November 16, 2018



[†]Department of Materials Science and Engineering, Cornell University, Ithaca, New York 14853, United States

^{*}School of Materials Science and Engineering, Nanyang Technological University, Singapore 639798, Singapore

[§]Department of Materials Science and Engineering, Beckman Institute for Advanced Science and Technology, University of Illinois at Urbana-Champaign, Urbana, Illinois 61801, United States

inverse morphology. 7,11,13,24,26-29 Mesoporous 3D continuous network morphologies are of particular interest for their high surface area, connectivity, pore accessibility, and mechanical stability and have been realized from silicates, transition-metal oxides, carbons, metals, and most recently, even from superconducting nitrides. 16,23,29-36 Such nanostructured materials often find their way into advanced applications. For example, BCP-directed bicontinuous gyroidal crystalline titania electrodes facilitate backfilling of the hole transport material through the interconnected pore network and enable continuous connectivity of the titania struts for enhanced electron collection and transport in dye-sensitized solar cells. 13 Moreover, it is desirable to construct a mesoporous BCP gyroid structure with high refractive index contrast to harness photonic properties of the chiral continuous network, for example, a single gyroidal mesoporous silicon (Si) nanostructure.3 Such Si network structures with 3D connectivity and high surface area may also be of interest for energy storage,1

hybrid photovoltaics,³⁷ and sensing applications.³⁸
We have previously demonstrated the generation of singlecrystal Si (semiconductor) and NiSi (metal) nanostructures connected epitaxially to the Si substrate by combining BCPdirected aluminosilicate/niobia hard templating, backfilling these mesoporous templates with amorphous precursors, and pulsed excimer laser annealing.²⁶ The critical step to achieve single-crystal epitaxy was to ensure a clean interface between the amorphous precursors and the Si substrate. However, in this early work, we have not yet been able to identify an ideal template material. (1) BCP-directed inorganic hybrid thin films are typically kinetically trapped in nonequilibrium-type morphologies after spin-coating because of rapid sol-gel condensation reactions, enhanced solvent evaporation during spin-coating, and interfacial energy contributions. 26,39 (2) Chemical inertness or highly selective etch resistance relative to SiO2 is required for complete native oxide removal on the single-crystal Si substrate. (3) Excellent template stability is necessary during the transient melt-crystallization process for high pattern transfer fidelity. 26 Recently, we have demonstrated that a mesoporous all-organic BCP-directed hybrid system may be able to fulfill all of the above requirements. First, BCP thin films with well-ordered periodic morphologies can be obtained by post-spin-coating treatments, including solvent or thermal annealing. 36,39-41 Second, many organic systems have high resistance to SiO₂ etchants (e.g., hydrofluoric (HF) acid). Third, the thermal stability of polymers is greatly enhanced during submillisecond CO2 transient laser heating up to 1000 °C. 27,42 However, the formation mechanism of self-assembled organic-template-derived crystalline Si nanostructures via nanosecond laser annealing remains elusive.

Here, we report a mechanistic study to establish the transient laser heating process-structure-property correlations of the generation of laser-induced crystalline Si (c-Si) network nanostructures via mesoporous all-organic BCPdirected template formation, backfilling with amorphous Si (a-Si), and nanosecond pulsed excimer laser annealing. We found that the organic mesoporous resin template materials properties were significantly enhanced as the laser-induced heating durations were reduced to the milli- to nanosecond timescales. Notably, the resin film network morphology remained stable up to the melting temperature of single-crystal Si at 1414 °C during submillisecond CO₂ laser heating in air. A dense a-Si overlayer on the resin template was essential to prevent excimer-laser-induced ablation effects. We further

employed grazing incidence small-angle X-ray scattering (GISAXS), coupled with scanning electron microscopy (SEM), to confirm good pattern transfer fidelity from the mesoporous organic template to inverse laser-induced c-Si nanostructures.

EXPERIMENTAL SECTION

Mesoporous BCP-Directed Resin Template Synthesis. ISOresol solutions (4, 6, and 8 wt %) were prepared by dissolving polyisoprene-block-polystyrene-block-poly(ethylene oxide) triblock terpolymer (PI-b-PS-b-PEO, ISO, $\hat{M}_n = 68.9$ kg mol⁻¹, with a polydispersity index of 1.04 containing 29.6 wt % PI, 64.8 wt % PS, and 5.6 wt % PEO) with resorcinol-formaldehyde resols (ISO/resols = 2.4:1, w/w) in anhydrous tetrahydrofuran (inhibitor-free, Sigma Aldrich) and stirred for 1 h. ISO terpolymer and resorcinolformaldehyde resols were synthesized according to protocols described elsewhere. ²³ All-organic hybrid thin films with a disordered network morphology were spin-coated on Si substrates (0.01–0.02 Ω cm, boron-doped, WRS Materials) at 2000 rpm (45 s) in a nitrogen dry box, followed by curing at 100 °C in a vacuum oven overnight (>12 h). The ISO-resol hybrid bulk samples with alternating gyroid morphology (ISO/resols = 3.125:1, w/w) were prepared by evaporation-induced self-assembly as reported elsewhere. 23 The gyroidal hybrid samples were sectioned with a Leica Ultracut UC7 cryoultramicrotome at -60 °C into thin films, which were collected on a water/dimethyl sulfoxide (6:4, v/v) solution surface and transferred to Si substrates. Mesoporous resin thin films were finally formed by heating the hybrid samples in a tube furnace at 450 °C (1 h) under nitrogen with a ramp rate of 1 °C min⁻¹. For Raman spectroscopy measurements, mesoporous resin samples were heated in a tube furnace at 600 °C (3 h) under nitrogen with a ramp rate of 1 °C min⁻¹ for carbonization.

Native SiO₂ Layer Removal and a-Si Chemical Vapor Deposition (CVD). The mesoporous resin samples were first immersed in a 0.5% hydrofluoric (HF) acid solution for ~2 min, blown dry with nitrogen, and immediately loaded into the CVD chamber under ambient conditions before chamber evacuation for a-Si deposition ($\sim 10^{-5}$ Torr). A static CVD system was used to deposit a-Si into the mesoporous resin template with disilane as the precursor at 350 °C (3 h).

CO₂ Laser (10.6 μ m) Transient Heating. The CO₂ laserinduced transient heating setup used in the experiments is described elsewhere. 42,43 The laser was focused to a line with a beam profile full width at half-maximum (FWHM) of 90 μ m by 600 μ m. For transient heating, this line beam was scanned across the sample surface at velocities of 45–1800 mm s⁻¹, resulting in 600 μ m FWHM scan lines with dwells of 0.05-2 ms. Mesoporous resin thin films with ~ 200 nm thickness were scanned with a single CO₂ laser irradiation at 28-92 W and dwells of 0.05, 0.2, 0.5, and 2 ms.

Pulsed Excimer Laser (308 nm) Annealing. The 40 ns pulsed XeCl excimer laser setup used here with some modifications is described elsewhere. 26,27 All samples were held in a small vacuum chamber holder (<1 Torr) with a quartz window for excimer laser irradiation. Mesoporous resin thin film samples were irradiated with a single pulse at fluences of 100 to 800 mJ cm⁻². The resin/a-Si composite samples with a disordered network morphology were irradiated with a single pulse at 700 mJ cm⁻². The gyroidal resin/a-Si composite samples were irradiated with a single pulse at fluences of 500 to 650 mJ cm⁻².

Resin Template Removal. The excimer-laser-irradiated samples were sequentially treated in CF₄ reactive ion etching (RIE) plasma for 10-20 s (30 sccm, 40 mTorr, 150 W) to remove the Si overlayer using an Oxford PlasmaLab 80+ RIE system, hot piranha solution $(97\% \text{ H}_2\text{SO}_4/30\% \text{ H}_2\text{O}_2 = 3:1, \text{v/v})$ held at 75 °C for 3 h to remove the template, and 49% HF for 10-30 s to remove the chemical SiO_2

Characterization. SEM images were acquired on Au-Pd-coated mesoporous resin samples and uncoated Si nanostructures using a LEO 1550 SEM equipped with an in-lens detector. Thin film **ACS Applied Materials & Interfaces**

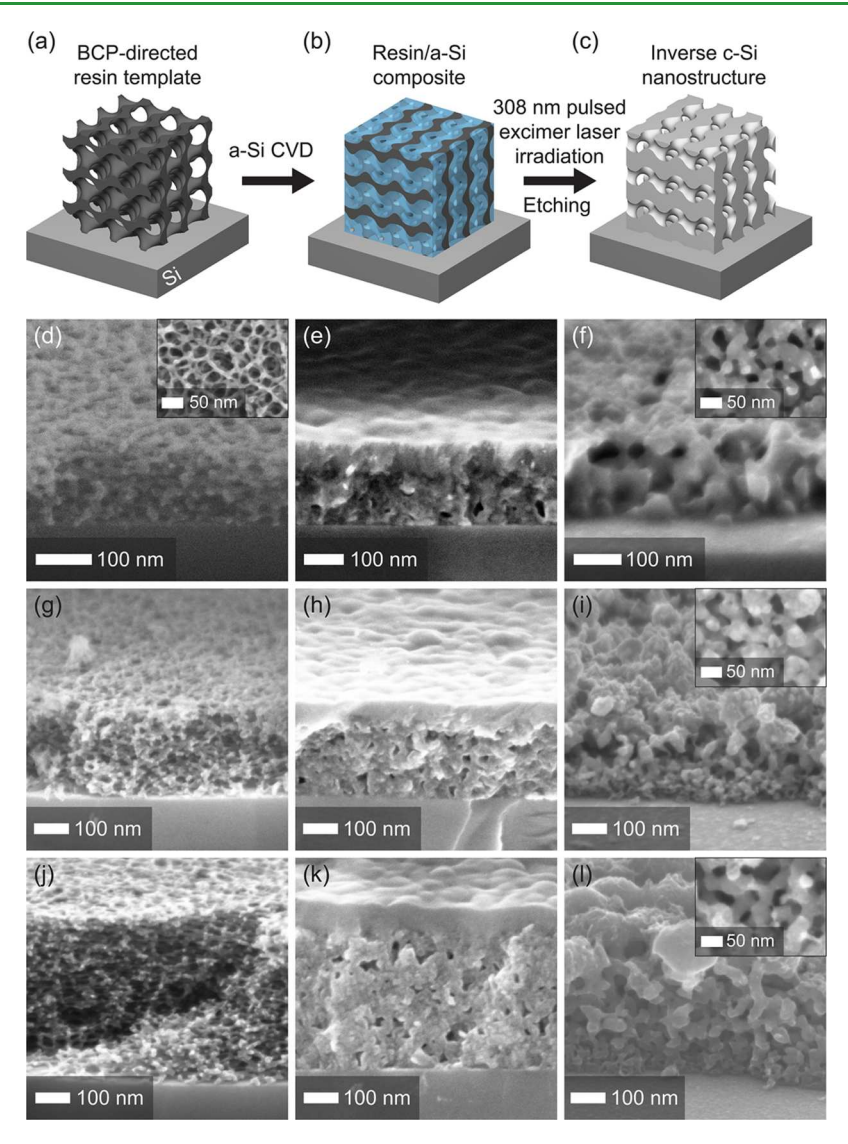


Figure 1. (a-c) Schematic illustration of steps in the transient pulsed XeCl excimer-laser-annealing-induced c-Si nanostructure formation process. (d-l) Cross-sectional and plan-view (insets) SEM micrographs of films at each stage of the process: (d, g, j) mesoporous BCP-directed resin templates with varying thickness after pyrolysis; (e, h, k) a-Si deposition into organic templates by CVD; (f, i, l) final inverse c-Si nanostructures after pulsed excimer laser irradiation and template removal.

thicknesses were determined from the SEM images (taking from N =8-60 cross section measurements) and a Tencor P-10 profilometer (number of measurements, $N \ge 3$). Pore size and strut width of the mesoporous resin films, as well as laser-induced c-Si network strut width, were determined from SEM images (taking from N = 79-200plan-view measurements). Raman spectroscopy measurements were conducted using a Renishaw InVia confocal Raman microscope with 488 and 785 nm excitation laser sources. Two-dimensional (2D) Xray diffraction (XRD) measurements were performed on a Bruker general area detector diffraction system (GADDS) equipped with a Bruker HI-STAR area detector using Cu K α radiation. GISAXS was measured at the G1 beamline of the Cornell High Energy Synchrotron Source. The G1 beamline setup consists of a multilayer monochromator of wavelength $\lambda = 1.18$ Å with a Dectris Pilatus 200k area detector mounted vertically at a distance of ~2.6 m from the sample. The resolution of the area detector was 487×407 pixels with a 172 μ m pixel size. The incident angle of the beam was varied between 0.1 and 0.3° with typical exposure times of <2 s. GISAXS patterns were analyzed with the FIT2D program.⁴⁴ Baseline removal was performed on the integrated intensity data using a smoothing spline fitting operation to data outside the peak region using the GenPlot software.

RESULTS AND DISCUSSION

Transient Nanosecond Pulsed XeCl Excimer-Laser-Annealing-Induced c-Si Nanostructure Formation. The transient laser-annealing-induced c-Si nanostructure formation process used here is shown schematically in Figure 1a-c. Allorganic hybrid thin films were spin-coated on a single-crystal Si substrate employing an ISO triblock terpolymer to structuredirect resorcinol-formaldehyde resol additives.²³ The resol oligomers were selectively attracted to the PEO block by hydrogen bonding. The all-organic hybrid thin films selfassembled into a disordered network morphology, as expected from the rapid solvent evaporation during the spin-coating process. After curing at 100 °C, the hybrid samples were pyrolyzed at 450 °C for 1 h under nitrogen. During pyrolysis, the cured resols cross-linked into phenolic resin, whereas the ISO terpolymer decomposed, yielding mesoporous BCPdirected resin thin films with a continuous network structure (Figure 1a).^{22,23} Mesoporous resin films of varying thickness were obtained by tailoring the ISO-resol solution concentration as shown via the SEM images in Figure 1d,g,j. After

immersing the mesoporous resin films in 0.5% HF acid solution for ~2 min to remove native oxide on the Si substrate, samples were immediately loaded into a static CVD chamber for a-Si deposition at 350 °C (see schematic in Figure 1b).⁴ SEM micrographs in Figure 1e,h,k show the near-complete backfilling of a-Si into the mesoporous resin templates with a 60-90 nm thick dense Si overlayer. The resin/a-Si composite films were then irradiated with a single 40 ns FWHM laser pulse at a 308 nm wavelength from a pulsed XeCl excimer laser at a 700 mJ cm⁻² fluence. The a-Si precursor absorbed most of the ultraviolet photons, melted, and subsequently solidified into c-Si within 50 ns, as confirmed by characteristic time-resolved reflectance measurements^{26,45,46} (Figure S1a, Supporting Information). Finally, porous inverse c-Si nanostructures were obtained after template removal by CF4 RIE and wet acid etching treatments as schematically depicted in Figure 1c and evidenced by SEM images shown in Figure 1f,i,l and Figure S2 (Supporting Information).

Plan-view and cross-sectional SEM micrographs in Figure 1d,g,j show mesoporous resin films with disordered continuous network structures of ~100, 200, and 400 nm thickness after pyrolysis, respectively, with interconnected pores both in-plane and out-of-plane. From SEM, the average pore diameter is 39 \pm 9 nm. GISAXS of the \sim 400 nm thick film shows two diffraction peaks at $q_{xy} = \pm 0.144 \text{ nm}^{-1}$, corresponding to a macroscopically homogeneous d spacing of $2\pi/q_{xy} = 43.6$ nm in the in-plane direction (Figure 2a), 15,47,48 with $q = \frac{4\pi \sin \theta}{10}$,

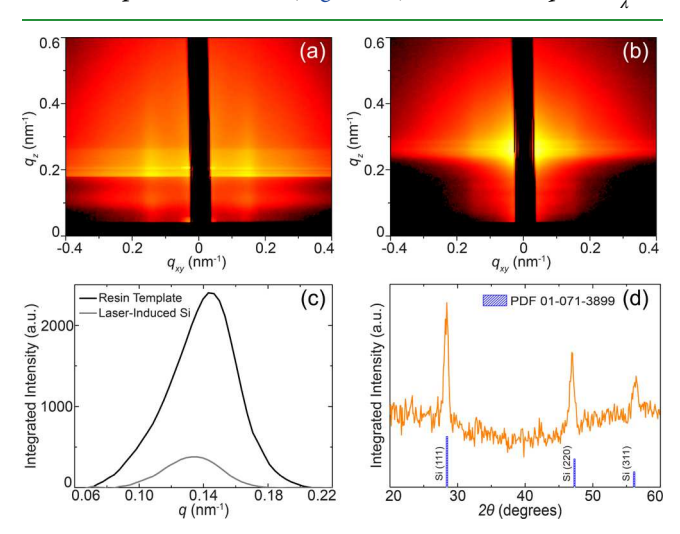


Figure 2. GISAXS profiles of (a) mesoporous resin template and corresponding (b) excimer-laser-induced c-Si nanostructure at incidence angles of 0.12 and 0.15°. (c) Azimuthally integrated intensity plots of corresponding GISAXS patterns. (d) GADDS integrated intensity plot of the excimer-laser-induced c-Si nanostructure after template removal. The peak markings and relative intensities for the expected crystalline Si (PDF 01-071-3899) are shown at the bottom.

where θ is half of the total scattering angle and λ is the X-ray wavelength (1.18 Å). The highly cross-linked resin exhibited remarkable materials properties throughout the hard templating and transient laser annealing processes. First, the chemically inert organic template remained highly stable during the ~2 min immersion in 0.5% HF acid solution with no observable film delamination. We further note that the a-Si CVD was performed directly on the thermally stable organic template at 350 °C without requiring an additional inorganic coating (e.g., SiO₂ or Al₂O₃) for stabilization.⁴ After pulsed excimer laser irradiation and template removal, SEM micrographs in Figure 1f,i,l (see also Figure S2) show that the final porous inverse c-Si network nanostructures were ~100 to 400 nm thick, that is, they had roughly the same thickness as the initial resin network structures. Closer examination at higher magnifications revealed characteristic features on mesoscopic length scales of the interconnected c-Si struts and pores. Figure 2b shows the GISAXS profile of a 350-400 nm thick inverse c-Si network structure film with two diffuse diffraction peaks at approximately $q_{xy}=\pm 0.134~{\rm nm}^{-1}$ corresponding to a macroscopically homogeneous d spacing of $2\pi/q_{xy}=46.9~{\rm nm}$ in the in-plane direction. From the integrated GISAXS intensity plots in Figure 2c, the close proximity of the scattering peaks (q = 0.144 versus 0.134 nm⁻¹) suggests a good degree of pattern transfer fidelity from the mesoporous resin template to the laser-induced inverse c-Si nanostructure. We note that the minor difference in the respective GISAXS peak position (\sim 7%) may be attributed to structural relaxation at high temperatures during the laser-induced silicon meltsolidification process. A slight expansion of the mesoporous template by inclusion of a-Si into the resin material during the CVD process cannot be excluded either. Importantly, the results of GISAXS measurements, with a millimeter-scale X-ray footprint coupled with local SEM characterization, suggest that the organic template retained its structural integrity during the transient melt-recrystallization of a-Si at temperatures >1250 °C. 45 In turn, this suggests that nanosecond-timeframe excimer laser heating suppresses oxidation reactions in ambient environments (in air), enabling organic systems to reach temperatures way beyond their conventional stability.

We conducted XRD using GADDS area scans to determine the crystal orientation texture of the excimer-laser-induced c-Si nanostructures as a function of 2θ scattering angle (radial distance) and azimuthal angle χ (angular distance) displayed in Figure S1b (Supporting Information). Despite immersing the organic template in 0.5% HF acid solution for ~2 min before a-Si CVD, the presence of scattering rings in the 2D GADDS profile (Figure S1b) indicates that the resulting excimer-laserinduced Si network nanostructures were polycrystalline. That is, the laser-induced nanostructured Si crystal orientation was not directed epitaxially by the substrate during the transient melt-solidification process.²⁶ The exact cause is currently unknown. As the CVD chamber lacked a load-lock mechanism, we speculate that a new native SiO2 layer may have grown on the Si substrate after the 0.5% HF treatment but before high vacuum was achieved in the deposition chamber.⁴ Raman spectroscopy (Figure S1c) and characteristic laser-induced "protruding and hillock" surface features 49-51 on the resultant mesoporous c-Si structures (see Figure 1f,i,j and Figure S2) further indicate complete melt-crystallization conversion of a-Si precursors into c-Si. The Scherrer formula, applied to the scattering peaks of the GADDS integrated intensity plot in Figure 2d, gives an estimated average Si crystallite size of 11 nm. From SEM, the average laser-induced c-Si strut width is 32 \pm 9 nm, suggesting that an average c-Si strut is spanned by \sim 3 crystallite domains.

Transient Submillisecond Continuous-Wave (CW) CO₂ Laser-Annealing-Induced Behavior of Organic **Templates.** To understand and correlate the thermal behavior of the organic template during short, rapid high-temperature exposures (e.g., transient heating during nanosecond pulsed excimer laser irradiation), we investigated the thermal stability **ACS Applied Materials & Interfaces**

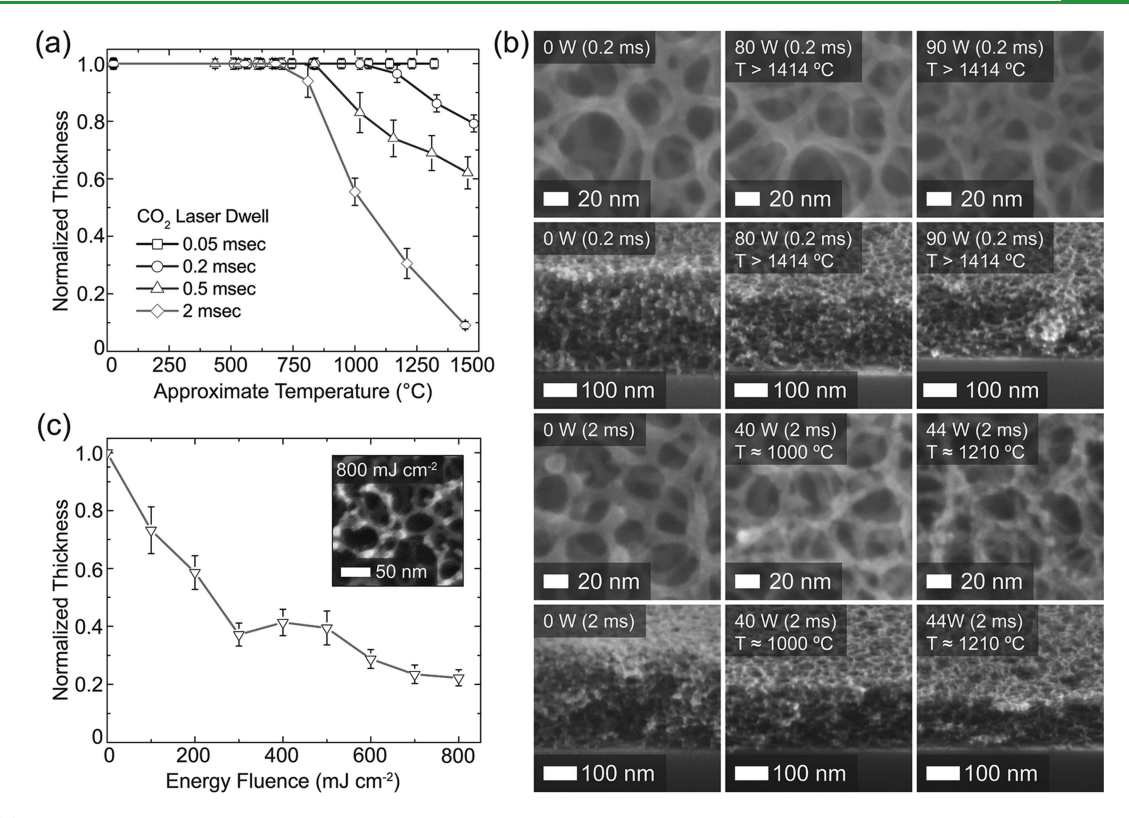


Figure 3. (a) Film thickness of mesoporous resin films versus transient laser heating temperature as obtained by a single CO2 laser irradiation of 0.05, 0.2, 0.5, and 2 ms dwells. (b) Plan-view (first and third rows) and cross-sectional (second and fourth rows) SEM micrographs of mesoporous resin structures after CO₂ laser-induced transient heating under conditions as indicated. (c) Film thickness of mesoporous resin films remaining after a single 40 ns pulsed XeCl excimer laser irradiation at fluences between 100 and 800 mJ cm⁻². Inset shows a plan-view SEM of a mesoporous resin structure after laser irradiation at the highest fluence of $800~\text{mJ}~\text{cm}^{-2}$.

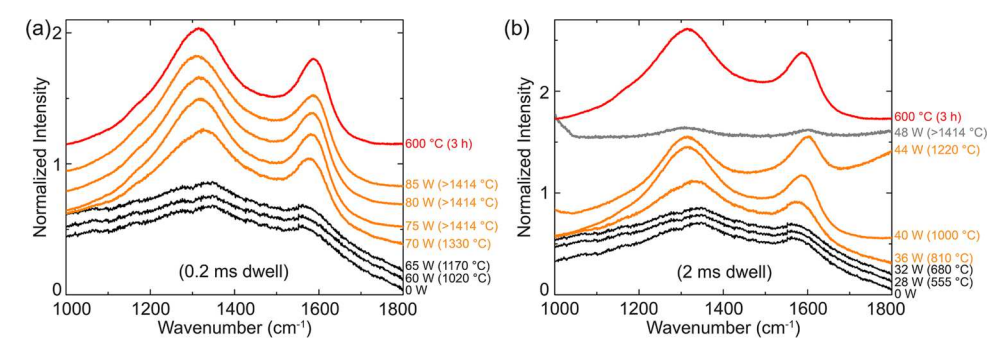


Figure 4. Raman spectra (785 nm excitation) of resin samples irradiated by CO₂ laser transient heating at (a) 0.2 and (b) 2 ms dwells. The red curves in the Raman spectra are from a mesoporous carbon sample carbonized in a tube furnace at 600 °C for 3 h under nitrogen as a reference.

of the mesoporous resin thin films on submillisecond time frames using a CW 10.6 μ m wavelength CO₂ laser. ^{42,43} The mesoporous resin film does not strongly interact with the farinfrared photons, but the highly boron-doped Si substrate does absorb the laser energy, thereby heating the film, which subsequently cools by thermal conduction on the millisecond time frames. 42,43 The transient temperature of the Si substrate during laser irradiation was determined from laser power and dwell times as described elsewhere. 42,43 Figure 3a (and Figure S3a, Supporting Information) shows the thickness of mesoporous resin thin films that remained after a single CO2 laser irradiation as a function of temperature (and laser power) for 0.05, 0.2, 0.5, and 2 ms dwells. The mesoporous resin samples survive the laser powers beyond the threshold for melting of the single-crystal Si substrate, that is, beyond temperatures of 1414 °C. Temperatures for such high laser

powers were approximated from empirical curves fitted to the laser power-temperature calibration data for different dwells. 42,43 From Figure 3a, it is clear that the thermal stability of the mesoporous resin samples increased substantially as the heating dwell time was reduced from 2 to 0.05 ms. Notably, the organic film thickness remained unchanged up to ~1320 °C for the 0.05 ms dwell. Near the melting temperature of single-crystal Si at 1414 °C, the film thickness decreased by \sim 20% for 0.2 ms, \sim 40% for 0.5 ms, and \sim 90% for 2 ms dwells. Despite the loss of film thickness at increasing dwells, representative SEM images of films after laser heating with 0.2 and 2 ms dwells at very high laser powers in Figure 3b confirmed that the CO₂ laser-irradiated samples retained their mesoporous network film morphology. From SEM, the original resin network strut width $(9.1 \pm 1.7 \text{ nm})$ after heating to the Si

melt temperature decreased by ~10 and 14% under 0.2 and 2 ms dwells, respectively.

We performed Raman spectroscopy on CO₂ laser-irradiated samples of 0.2 and 2 ms dwells to investigate the associated chemical changes during milli- to submillisecond laser heating as shown in Figure 4. Before CO₂ laser irradiation (0 W), broad D and G bands around 1340 and 1560 cm⁻¹, respectively, were detected for mesoporous resin samples pyrolyzed at 450 °C. The bands shifted and became narrower as the laser power increased, suggesting that the transient laser heating induced carbonization of the phenolic resin into disordered carbon. 22,23 The Raman spectra of samples irradiated at 75 W of 0.2 ms dwell (T > 1414 °C) and 40 W of 2 ms dwell ($T \approx 1000 \, ^{\circ}\text{C}$) in Figure 4a,b, respectively, are essentially identical to the Raman spectrum of a mesoporous disordered carbon film furnace carbonized at 600 °C for 3 h under nitrogen. As expected from the results in Figure 3a, the longer the dwell time, the lower the threshold laser power, beyond which the film degrades. Moving beyond 40 W for the 2 ms dwell, for example, 48 W of 2 ms dwell (T >1414 °C), thermal decomposition resulted in a significant film thickness loss (Figure 3a) and diminished Raman spectrum intensities (Figure 4b). Putting it in a different way, Raman results in Figure 4 demonstrate that the shorter the dwell time, the higher temperature processing these resin films can tolerate.

The behavior from submillisecond transient laser heating (CO₂ laser) can be compared with that from nanosecond heating (excimer laser). Figure 3c shows the evolution of the thickness of the mesoporous resin template after a single 40 ns pulsed excimer laser irradiation at fluences between 100 and 800 mJ cm⁻² (no temperature calibration available). We observed a rapid film thickness loss of over 60% from 100 to 300 mJ cm⁻² and a more gradual decrease to almost 80% for fluences between 300 and 800 mJ cm⁻². We hypothesize that the thickness loss is partially due to ablation of phenolic resin that readily absorbs the ultraviolet excimer laser irradiation 52,53 and is heated transiently to temperatures beyond the melting point of Si. Raman spectroscopy indicated that the mesoporous films were laser-carbonized along with a ~30% film thickness loss at 100 mJ cm⁻² (Figure S3b). Whereas the excimer-laser-irradiated resin films retained mesoporous structural features for all laser fluences up to 800 mJ cm⁻² (see plan-view SEM inset in Figure 3c and Figure S3c-f), Raman intensities in the spectra vanished for samples irradiated with fluences from 200 mJ cm⁻² onward possibly because of substantially increased surface roughness (see crosssectional images in Figure S3g-j).

The dense a-Si overlayer observed in the images in Figure 1e,h,k plays a critical role in the successful 3D pattern transfer from the mesoporous resin template to the excimer-laserinduced c-Si nanostructures. Upon laser irradiation at 700 mJ cm⁻², most of the photons are absorbed by the a-Si overlayer and converted into thermal energy to induce Si melting as indicated by the sharp spike in time-resolved reflectance measurements (Figure S1a). 26,27,45,46 As the Si melt front propagates through the a-Si into the substrate, the resin scaffold is carbonized and acts as a "hard" support for liquid Si that subsequently solidifies within 40-50 ns. 34-56 In control experiments, the a-Si overlayer was removed by CF₄ RIE before pulsed excimer laser annealing. Indeed, we observed no mesoporous structural features after laser annealing and template removal for control samples with little or no a-Si

overlayer, confirming the critical role of the dense a-Si overlayer (Figure S4, Supporting Information). Some photons (e.g., at the 700 mJ cm⁻² fluence) may still be absorbed by the resin material causing ablation near the top of the mesoporous organic template. This results in the formation of asymmetric laser-induced c-Si network nanostructures with graded nanoporosity. In Figure 1f,i,l (and Figure S2), the largest pores are observed at the air/Si interface and become increasingly smaller toward the Si substrate interface, especially for the thicker films (compare Figure 1f with Figure 1i,l).

Proof-of-Principle Experiments To Generate Periodically Ordered Laser-Induced c-Si Nanostructures. As discussed in the Introduction, one of the advantages of working with all-organic as compared to inorganic thin film templates is the accessibility of well-ordered complex 3D BCP template structures, which subsequently can be transferred into the corresponding c-Si structures via pulsed excimer laser annealing. To demonstrate the potential of this approach, we performed proof-of-principle experiments to generate the first periodically ordered laser-induced c-Si nanostructures by BCPdirected organic templating.²⁷ BCP gyroid structures usually consist of two interpenetrating gyroidal subvolumes related by an inversion operation. If these two subvolumes are constituted by the same material (e.g., in AB di-BCPs), the structure is referred to as a double gyroid $(Ia\overline{3}d)$. In the case where the two subvolumes are made up of different materials (e.g., in ABC triblock terpolymers), the structure is called the alternating (or single) gyroid (I4₁32).^{32,58}

For our experiments, bulk ISO-resol hybrid samples with an alternating gyroid morphology were first prepared by evaporation-induced self-assembly. Subsequently, 700–900 nm-thick cryomicrotomed sections of the gyroidal all-organic hybrid samples were collected on Si substrates. SEM images in Figure 5a,b show a highly porous resin thin film with a mesoscopic gyroidal network morphology obtained after removing the ISO terpolymer by pyrolysis at 450 °C for 1 h under nitrogen. Lower-magnification SEM images in Figure S5 (Supporting Information) demonstrate that the gyroidal mesoporous resin thin film sections adhered smoothly on the Si substrate, which we attributed to the "soft" nature of the allorganic hybrid thin films. We note that GISAXS measurements were not conducted for the mesoporous gyroidal resin templates because of the nonuniform coverage of cryomicrotomed sections on the substrates. SEM images in Figure 5c,d, as well as in Figure 6, demonstrate that periodically ordered 3D porous inverse c-Si nanostructures could be obtained after a-Si CVD, a single pulsed excimer laser irradiation at fluences of 500 to 650 mJ cm⁻², and template removal.

Plan-view and cross-sectional SEM micrographs suggest that the interconnected and periodic pores of the mesoporous gyroidal resin template (Figure 5a,b) were conformally backfilled during this process, resulting in excimer-laserinduced c-Si nanostructures (Figure 5c,d). However, crosssectional SEM images of other laser annealed areas in Figure 6 reveal that the excimer-laser-induced melt-crystallization of Si was incomplete as the bottom half to one third of the samples show a dense a-Si layer. Despite only having more than half of the backfilled a-Si transform into periodically ordered c-Si nanostructures by laser-induced melt infiltration, 59 these proofof-concept experiments demonstrate the possibility to generate highly ordered and periodic c-Si nanostructures by combining mesoporous all-organic BCP-directed templating with pulsed excimer laser annealing.

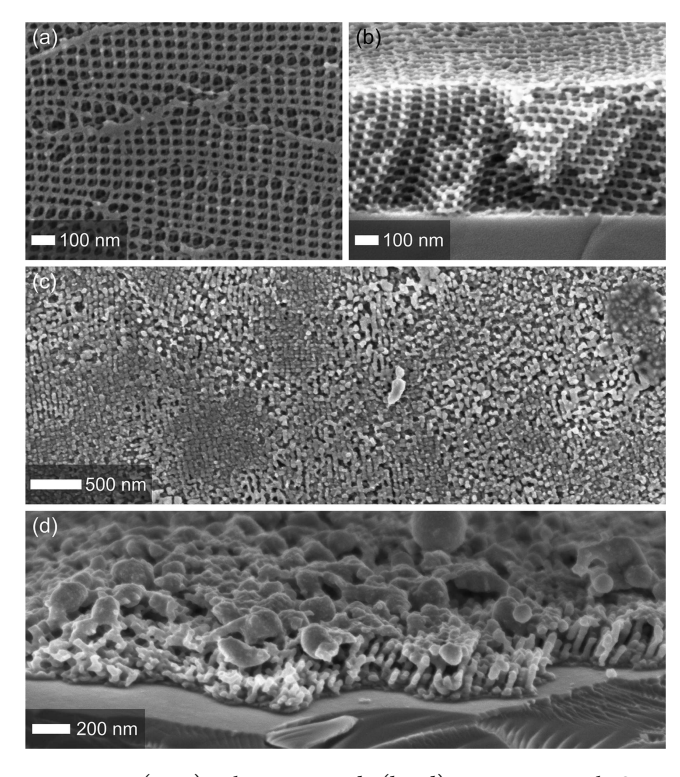


Figure 5. (a, c) Plan-view and (b, d) cross-sectional SEM micrographs of (a, b) cryomicrotomed gyroidal mesoporous resin template after pyrolysis, and (c, d) different areas of corresponding periodically ordered c-Si nanostructures after a single pulsed excimer laser irradiation at fluences of (c) 500 and (d) 650 mJ cm⁻² and subsequent template removal.

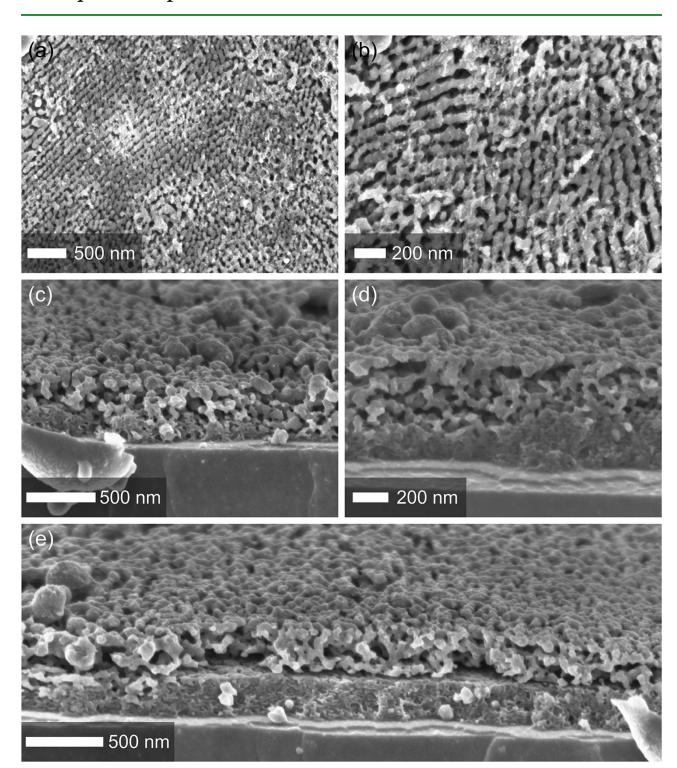


Figure 6. (a, b) Plan-view and (c-e) cross-sectional SEM micrographs showing various areas of ordered laser-induced c-Si nanostructures after a single excimer laser irradiation at fluences of (a, b) 550 and (c-e) 500 mJ cm⁻² and template removal.

CONCLUSIONS

In summary, we have described the detailed investigation of coupling mesoporous all-organic BCP-directed resin templating with a-Si CVD and transient excimer-laser-induced meltcrystallization to generate 3D porous c-Si network nanostructures. A dense a-Si overlayer was critical to shield the mesoporous resin template from strongly absorbing the 308 nm pulsed excimer laser irradiation to prevent template ablation and structural collapse. To establish transient laser heating process-structure-property correlations, mesoporous resin templates were heated in air with a 10.6 μ m CO₂ laser on milli- to submillisecond timescales and found to remain highly stable up to the melting temperature of single-crystal Si (1414 °C). Raman spectroscopy revealed that the mesoporous resin scaffold material was carbonized during transient heating in air, thereby imparting enhanced thermal and structural stability to support the excimer-laser-induced Si melt-crystallization to form 3D porous c-Si nanostructures. Millimeter-scale GISAXS coupled with local SEM affirmed that the excimer-laserinduced nanopattern transfer yields were high. Besides disordered network structures, we demonstrated that the transition from BCP-directed inorganic to organic templating enables the formation of periodically ordered c-Si nanostructures via pulsed laser annealing. We expect that the methodology outlined here can be further enhanced, for example, by directly achieving periodically ordered morphologies in ISO-resol hybrid thin films by thermal or solvent annealing before mesoporous resin structure formation. 36,39-Finally, by preventing the formation of any SiO₂ on the Si substrate before a-Si deposition, it should be possible to generate mesoporous single-crystal epitaxial Si nanostructures²⁶ with different periodically ordered morphologies that may enable new functionalities and advanced applications.

ASSOCIATED CONTENT

S Supporting Information

The Supporting Information is available free of charge on the ACS Publications website at DOI: 10.1021/acsami.8b12706.

Additional characterization data from SEM, Raman spectroscopy and X-ray diffraction, and time-resolved reflectance data and mesoporous resin film thickness measurements (PDF)

AUTHOR INFORMATION

Corresponding Author

*E-mail: ubw1@cornell.edu.

ORCID ®

Kwan Wee Tan: 0000-0002-8289-6503 Jörg G. Werner: 0000-0001-7845-086X Hiroaki Sai: 0000-0002-4268-2148 Paul V. Braun: 0000-0003-4079-8160 Ulrich Wiesner: 0000-0001-6934-3755

Author Contributions

All authors have given approval to the final version of the manuscript.

Notes

The authors declare no competing financial interest.

ACKNOWLEDGMENTS

This work was supported by the National Science Foundation (NSF) Single Investigator Award (DMR-1707836). This work

made use of research facilities at Cornell Center for Materials Research with support from the NSF Materials Research Science and Engineering Centers program (DMR-1719875); Cornell NanoScale Science & Technology Facility, a member of the National Nanotechnology Coordinated Infrastructure, which is supported by the NSF (Grant ECCS-1542081); and Cornell High Energy Synchrotron Source supported by the National Science Foundation under award DMR-1332208. The work at the University of Illinois was supported by Air Force Office of Scientific Research MURI FA9550-12-1-0471. K.W.T. acknowledges the Singapore Ministry of Education AcRF Tier 1 grant (2018-T1-001-084) and a startup grant from Nanyang Technological University, Singapore. The authors gratefully acknowledge Prof. L. Estroff, Dr. M. Weathers, Dr. R. Bell, and Dr. A. Jacobs of Cornell University for their kind experimental assistance and helpful discussions.

REFERENCES

- (1) Lu, A.-H.; Zhao, D.; Wan, Y. Principles of Nanocasting. In Nanocasting: A Versatile Strategy for Creating Nanostructured Porous Materials; Royal Society of Chemistry: Cambridge, U.K., 2009; pp 1-
- (2) Vlasov, Y. A.; Bo, X.-Z.; Sturm, J. C.; Norris, D. J. On-Chip Natural Assembly of Silicon Photonic Bandgap Crystals. Nature 2001, 414, 289-293.
- (3) Urbas, A. M.; Maldovan, M.; DeRege, P.; Thomas, E. L. Bicontinuous Cubic Block Copolymer Photonic Crystals. Adv. Mater. 2002, 14, 1850-1853.
- (4) Rinne, S. A.; García-Santamaría, F.; Braun, P. V. Embedded Cavities and Waveguides in Three-Dimensional Silicon Photonic Crystals. Nat. Photonics 2008, 2, 52-56.
- (5) Nelson, E. C.; Dias, N. L.; Bassett, K. P.; Dunham, S. N.; Verma, V.; Miyake, M.; Wiltzius, P.; Rogers, J. A.; Coleman, J. J.; Li, X.; Braun, P. V. Epitaxial Growth of Three-Dimensionally Architectured Optoelectronic Devices. Nat. Mater. 2011, 10, 676-681.
- (6) Hur, K.; Francescato, Y.; Giannini, V.; Maier, S. A.; Hennig, R. G.; Wiesner, U. Three-Dimensionally Isotropic Negative Refractive Index Materials from Block Copolymer Self-Assembled Chiral Gyroid Networks. Angew. Chem. Int. Ed. 2011, 50, 11985-11989.
- (7) Vignolini, S.; Yufa, N. A.; Cunha, P. S.; Guldin, S.; Rushkin, I.; Stefik, M.; Hur, K.; Wiesner, U.; Baumberg, J. J.; Steiner, U. A 3D Optical Metamaterial Made by Self-Assembly. Adv. Mater. 2012, 24,
- (8) Van Gough, D.; Juhl, A. T.; Braun, P. V. Programming Structure into 3D Nanomaterials. Mater. Today 2009, 12, 28-35.
- (9) Orilall, M. C.; Wiesner, U. Block Copolymer Based Composition and Morphology Control in Nanostructured Hybrid Materials for Energy Conversion and Storage: Solar Cells, Batteries, and Fuel Cells. Chem. Soc. Rev. 2011, 40, 520-535.
- (10) Ross, C. A.; Berggren, K. K.; Cheng, J. Y.; Jung, Y. S.; Chang, J.-B. Three-Dimensional Nanofabrication by Block Copolymer Self-Assembly. Adv. Mater. 2014, 26, 4386-4396.
- (11) Joo, S. H.; Choi, S. J.; Oh, I.; Kwak, J.; Liu, Z.; Terasaki, O.; Ryoo, R. Ordered Nanoporous Arrays of Carbon Supporting High Dispersions of Platinum Nanoparticles. Nature 2001, 412, 169-172.
- (12) Kibsgaard, J.; Chen, Z.; Reinecke, B. N.; Jaramillo, T. F. Engineering the Surface Structure of MoS₂ to Preferentially Expose Active Edge Sites for Electrocatalysis. Nat. Mater. 2012, 11, 963-969.
- (13) Crossland, E. J. W.; Kamperman, M.; Nedelcu, M.; Ducati, C.; Wiesner, U.; Smilgies, D.-M.; Toombes, G. E. S.; Hillmyer, M. A.; Ludwigs, S.; Steiner, U.; Snaith, H. J. A Bicontinuous Double Gyroid Hybrid Solar Cell. Nano Lett. 2009, 9, 2807-2812.
- (14) Zhang, H.; Braun, P. V. Three-Dimensional Metal Scaffold Supported Bicontinuous Silicon Battery Anodes. Nano Lett. 2012, 12, 2778 - 2783.
- (15) Tan, K. W.; Moore, D. T.; Saliba, M.; Sai, H.; Estroff, L. A.; Hanrath, T.; Snaith, H. J.; Wiesner, U. Thermally Induced Structural

- Evolution and Performance of Mesoporous Block Copolymer-Directed Alumina Perovskite Solar Cells. ACS Nano 2014, 8, 4730-4739.
- (16) Werner, J. G.; Johnson, S. S.; Vijay, V.; Wiesner, U. Carbon-Sulfur Composites from Cylindrical and Gyroidal Mesoporous Carbons with Tunable Properties in Lithium-Sulfur Batteries. Chem. Mater. 2015, 27, 3349-3357.
- (17) Werner, J. G.; Rodríguez-Calero, G. G.; Abruña, H. D.; Wiesner, U. Block Copolymer Derived 3-D Interpenetrating Multifunctional Gyroidal Nanohybrids for Electrical Energy Storage. Energy Environ. Sci. 2018, 11, 1261-1270.
- (18) Templin, M.; Franck, A.; Chesne, A. D.; Leist, H.; Zhang, Y.; Ulrich, R.; Schädler, V.; Wiesner, U. Organically Modified Aluminosilicate Mesostructures from Block Copolymer Phases. Science 1997, 278, 1795-1798.
- (19) Zhao, D.; Feng, J.; Huo, Q.; Melosh, N.; Fredrickson, G. H.; Chmelka, B. F.; Stucky, G. D. Triblock Copolymer Syntheses of Mesoporous Silica with Periodic 50 to 300 Angstrom Pores. Science 1998, 279, 548-552.
- (20) Yang, P.; Zhao, D.; Margolese, D. I.; Chmelka, B. F.; Stucky, G. D. Generalized Syntheses of Large-Pore Mesoporous Metal Oxides with Semicrystalline Frameworks. Nature 1998, 396, 152-155.
- (21) Warren, S. C.; Messina, L. C.; Slaughter, L. S.; Kamperman, M.; Zhou, Q.; Gruner, S. M.; DiSalvo, F. J.; Wiesner, U. Ordered Mesoporous Materials from Metal Nanoparticle-Block Copolymer Self-Assembly. Science 2008, 320, 1748-1752.
- (22) Meng, Y.; Gu, D.; Zhang, F.; Shi, Y.; Cheng, L.; Feng, D.; Wu, Z.; Chen, Z.; Wan, Y.; Stein, A.; Zhao, D. A Family of Highly Ordered Mesoporous Polymer Resin and Carbon Structures from Organicorganic Self-Assembly. Chem. Mater. 2006, 18, 4447-4464.
- (23) Werner, J. G.; Hoheisel, T. N.; Wiesner, U. Synthesis and Characterization of Gyroidal Mesoporous Carbons and Carbon Monoliths with Tunable Ultralarge Pore Size. ACS Nano 2014, 8, 731-743.
- (24) Sai, H.; Tan, K. W.; Hur, K.; Asenath-Smith, E.; Hovden, R.; Jiang, Y.; Riccio, M.; Muller, D. A.; Elser, V.; Estroff, L. A.; Gruner, S. M.; Wiesner, U. Hierarchical Porous Polymer Scaffolds from Block Copolymers. Science 2013, 341, 530-534.
- (25) Hoheisel, T. N.; Hur, K.; Wiesner, U. B. Block Copolymer-Nanoparticle Hybrid Self-Assembly. Prog. Polym. Sci. 2015, 40, 3-32. (26) Arora, H.; Du, P.; Tan, K. W.; Hyun, J. K.; Grazul, J.; Xin, H. L.; Muller, D. A.; Thompson, M. O.; Wiesner, U. Block Copolymer Self-Assembly-Directed Single-Crystal Homo- and Heteroepitaxial Nanostructures. Science 2010, 330, 214-219.
- (27) Tan, K. W.; Jung, B.; Werner, J. G.; Rhoades, E. R.; Thompson, M. O.; Wiesner, U. Transient Laser Heating Induced Hierarchical Porous Structures from Block Copolymer-Directed Self-Assembly. Science 2015, 349, 54-58.
- (28) Gu, Y.; Werner, J. G.; Dorin, R. M.; Robbins, S. W.; Wiesner, U. Graded Porous Inorganic Materials Derived from Self-Assembled Block Copolymer Templates. Nanoscale 2015, 7, 5826-5834.
- (29) Hsueh, H.-Y.; Huang, Y.-C.; Ho, R.-M.; Lai, C.-H.; Makida, T.; Hasegawa, H. Nanoporous Gyroid Nickel from Block Copolymer Templates via Electroless Plating. Adv. Mater. 2011, 23, 3041-3046.
- (30) Toombes, G. E. S.; Finnefrock, A. C.; Tate, M. W.; Ulrich, R.; Wiesner, U.; Gruner, S. M. A Re-Evaluation of the Morphology of a Bicontinuous Block Copolymer-Ceramic Material. Macromolecules 2007, 40, 8974-8982.
- (31) Stefik, M.; Wang, S.; Hovden, R.; Sai, H.; Tate, M. W.; Muller, D. A.; Steiner, U.; Gruner, S. M.; Wiesner, U. Networked and Chiral Nanocomposites from ABC Triblock Terpolymer Coassembly with Transition Metal Oxide Nanoparticles. J. Mater. Chem. 2012, 22, 1078-1087.
- (32) Li, Z.; Hur, K.; Sai, H.; Higuchi, T.; Takahara, A.; Jinnai, H.; Gruner, S. M.; Wiesner, U. Linking Experiment and Theory for Three-Dimensional Networked Binary Metal Nanoparticle-Triblock Terpolymer Superstructures. Nat. Commun. 2014, 5, 3247.

- (33) Robbins, S. W.; Sai, H.; DiSalvo, F. J.; Gruner, S. M.; Wiesner, U. Monolithic Gyroidal Mesoporous Mixed Titanium—Niobium Nitrides. *ACS Nano* **2014**, *8*, 8217—8223.
- (34) Robbins, S. W.; Beaucage, P. A.; Sai, H.; Tan, K. W.; Werner, J. G.; Sethna, J. P.; DiSalvo, F. J.; Gruner, S. M.; Dover, R. B. V.; Wiesner, U. Block Copolymer Self-Assembly—Directed Synthesis of Mesoporous Gyroidal Superconductors. *Sci. Adv.* **2016**, *2*, e1501119.
- (35) Susca, E. M.; Beaucage, P. A.; Hanson, M. A.; Werner-Zwanziger, U.; Zwanziger, J. W.; Estroff, L. A.; Wiesner, U. Self-Assembled Gyroidal Mesoporous Polymer-Derived High Temperature Ceramic Monoliths. *Chem. Mater.* **2016**, *28*, 2131–2137.
- (36) Zhang, Q.; Matsuoka, F.; Suh, H. S.; Beaucage, P. A.; Xiong, S.; Smilgies, D.-M.; Tan, K. W.; Werner, J. G.; Nealey, P. F.; Wiesner, U. B. Pathways to Mesoporous Resin/Carbon Thin Films with Alternating Gyroid Morphology. ACS Nano 2018, 12, 347–358.
- (37) Sahli, F.; Werner, J.; Kamino, B. A.; Bräuninger, M.; Monnard, R.; Paviet-Salomon, B.; Barraud, L.; Ding, L.; Leon, J. J. D.; Sacchetto, D.; Cattaneo, G.; Despeisse, M.; Boccard, M.; Nicolay, S.; Jeangros, Q.; Niesen, B.; Ballif, C. Fully Textured Monolithic Perovskite/Silicon Tandem Solar Cells with 25.2% Power Conversion Efficiency. *Nat. Mater.* 2018, 17, 820–826.
- (38) Bao, Z.; Weatherspoon, M. R.; Shian, S.; Cai, Y.; Graham, P. D.; Allan, S. M.; Ahmad, G.; Dickerson, M. B.; Church, B. C.; Kang, Z.; Abernathy, H. W., III; Summers, C. J.; Liu, M.; Sandhage, K. H. Chemical Reduction of Three-Dimensional Silica Micro-Assemblies into Microporous Silicon Replicas. *Nature* **2007**, *446*, 172–175.
- (39) Albert, J. N. L.; Epps, T. H., III Self-Assembly of Block Copolymer Thin Films. *Mater. Today* **2010**, *13*, 24–33.
- (40) Park, S.; Lee, D. H.; Xu, J.; Kim, B.; Hong, S. W.; Jeong, U.; Xu, T.; Russell, T. P. Macroscopic 10-Terabit—per—Square-Inch Arrays from Block Copolymers with Lateral Order. *Science* **2009**, *323*, 1030—1033.
- (41) Deng, G.; Zhang, Y.; Ye, C.; Qiang, Z.; Stein, G. E.; Cavicchi, K. A.; Vogt, B. D. Bicontinuous Mesoporous Carbon Thin Films via an Order-Order Transition. *Chem. Commun.* **2014**, *50*, 12684–12687.
- (42) Jung, B.; Sha, J.; Paredes, F.; Chandhok, M.; Younkin, T. R.; Wiesner, U.; Ober, C. K.; Thompson, M. O. Kinetic Rates of Thermal Transformations and Diffusion in Polymer Systems Measured during Sub-Millisecond Laser-Induced Heating. *ACS Nano* **2012**, *6*, 5830–5836
- (43) Iyengar, K.; Jung, B.; Willemann, M.; Clancy, P.; Thompson, M. O. Experimental Determination of Thermal Profiles during Laser Spike Annealing with Quantitative Comparison to 3-Dimensional Simulations. *Appl. Phys. Lett.* **2012**, *100*, 211915.
- (44) Hammersley, A. P.; Svensson, S. O.; Hanfland, M.; Fitch, A. N.; Hausermann, D. Two-Dimensional Detector Software: From Real Detector to Idealised Image or Two-Theta Scan. *High Pressure Res.* **1996**, *14*, 235–248.
- (45) Thompson, M. O.; Galvin, G. J.; Mayer, J. W.; Peercy, P. S.; Poate, J. M.; Jacobson, D. C.; Cullis, A. G.; Chew, N. G. Melting Temperature and Explosive Crystallization of Amorphous Silicon during Pulsed Laser Irradiation. *Phys. Rev. Lett.* **1984**, 52, 2360–2363.
- (46) Auston, D. H.; Surko, C. M.; Venkatesan, T. N. C.; Slusher, R. E.; Golovchenko, J. A. Time-resolved Reflectivity of Ion-implanted Silicon during Laser Annealing. *Appl. Phys. Lett.* **1978**, 33, 437–440.
- (47) Rauda, I. E.; Buonsanti, R.; Saldarriaga-Lopez, L. C.; Benjauthrit, K.; Schelhas, L. T.; Stefik, M.; Augustyn, V.; Ko, J.; Dunn, B.; Wiesner, U.; Milliron, D. J.; Tolbert, S. H. General Method for the Synthesis of Hierarchical Nanocrystal-Based Mesoporous Materials. ACS Nano 2012, 6, 6386–6399.
- (48) Busch, P.; Rauscher, M.; Smilgies, D.-M.; Posselt, D.; Papadakis, C. M. Grazing-Incidence Small-Angle X-Ray Scattering from Thin Polymer Films with Lamellar Structures the Scattering Cross Section in the Distorted-Wave Born Approximation. *J. Appl. Crystallogr.* **2006**, 39, 433—442.
- (49) Fork, D. K.; Anderson, G. B.; Boyce, J. B.; Johnson, R. I.; Mei, P. Capillary Waves in Pulsed Excimer Laser Crystallized Amorphous Silicon. *Appl. Phys. Lett.* **1996**, *68*, 2138–2140.

- (50) Street, R., Ed. *Technology and Applications of Amorphous Silicon*; Springer Series in Materials Science; Springer-Verlag: Berlin, Germany, 2000, DOI: 10.1007/978-3-662-04141-3.
- (51) Tan, K. W.; Saba, S. A.; Arora, H.; Thompson, M. O.; Wiesner, U. Colloidal Self-Assembly-Directed Laser-Induced Non-Close-Packed Crystalline Silicon Nanostructures. *ACS Nano* **2011**, *5*, 7960–7966.
- (52) Pretsch, E.; Bühlmann, P.; Badertscher, M. Summary Tables. In Structure Determination of Organic Compounds: Tables of Spectral Data; Springer Berlin Heidelberg: Berlin, Germany, 2009; pp 46–47, DOI: 10.1007/978-3-540-93810-1 2.
- (53) Urech, L.; Lippert, T. Photoablation of Polymer Materials. In *Photochemistry and Photophysics of Polymer Materials*; Allen, N. S., Ed.; John Wiley & Sons, Inc., 2010; pp 541–568, DOI: 10.1002/9780470594179.ch14.
- (54) Katou, T.; Lee, B.; Lu, D.; Kondo, J. N.; Hara, M.; Domen, K. Crystallization of an Ordered Mesoporous Nb-Ta Oxide. *Angew. Chem. Int. Ed.* **2003**, *42*, 2382–2385.
- (55) Lee, J.; Orilall, M. C.; Warren, S. C.; Kamperman, M.; DiSalvo, F. J.; Wiesner, U. Direct Access to Thermally Stable and Highly Crystalline Mesoporous Transition-Metal Oxides with Uniform Pores. *Nat. Mater.* **2008**, *7*, 222–228.
- (56) Tan, K. W.; Sai, H.; Robbins, S. W.; Werner, J. G.; Hoheisel, T. N.; Hesse, S. A.; Beaucage, P. A.; DiSalvo, F. J.; Gruner, S. M.; Murtagh, M.; Wiesner, U. Ordered Mesoporous Crystalline Aluminas from Self-Assembly of ABC Triblock Terpolymer—Butanol—Alumina Sols. RSC Adv. 2015, 5, 49287—49294.
- (57) Schoen, A. H. Infinite Periodic Minimal Surfaces without Self-Intersections; NASA Technical Note, NASA TN D-5541; NASA Electronics Research Center: Cambridge, MA, 1970.
- (58) Epps, T. H., III; Cochran, E. W.; Bailey, T. S.; Waletzko, R. S.; Hardy, C. M.; Bates, F. S. Ordered Network Phases in Linear Poly(isoprene-b-styrene-b-ethylene oxide) Triblock Copolymers. *Macromolecules* **2004**, *37*, 8325–8341.
- (59) de Jongh, P. E.; Eggenhuisen, T. M. Melt Infiltration: An Emerging Technique for the Preparation of Novel Functional Nanostructured Materials. *Adv. Mater.* **2013**, *25*, 6672–6690.